Can we get the best of both Binary Neural Networks and Spiking Neural Networks for Efficient Computer Vision?

Gourav Datta[*,†], **Zeyu Liu**[*], **Peter A. Beerel**
University of Southern California, Los Angeles, CA, USA
{gdatta,liuzeyu,pabeerel}@usc.edu
[*]Equally contributing authors [†]Currently employed at Amazon Inc.

Abstract

Binary Neural networks (BNN) have emerged as an attractive computing paradigm for a wide range of low-power vision tasks. However, state-of-the-art (SOTA) BNNs do not yield any sparsity, and induce a significant number of non-binary operations. On the other hand, activation sparsity can be provided by spiking neural networks (SNN), that too have gained significant traction in recent times. Thanks to this sparsity, SNNs when implemented on neuromorphic hardware, have the potential to be significantly more power-efficient compared to traditional artifical neural networks (ANN). However, SNNs incur multiple time steps to achieve close to SOTA accuracy. Ironically, this increases latency and energy—costs that SNNs were proposed to reduce—and presents itself as a major hurdle in realizing SNNs' theoretical gains in practice. This raises an intriguing question: *Can we obtain SNN-like sparsity and BNN-like accuracy and enjoy the energy-efficiency benefits of both?* To answer this question, in this paper, we present a training framework for sparse binary activation neural networks (BANN) using a novel variant of the Hoyer regularizer. We estimate the threshold of each BANN layer as the Hoyer extremum of a clipped version of its activation map, where the clipping value is trained using gradient descent with our Hoyer regularizer. This approach shifts the activation values away from the threshold, thereby mitigating the effect of noise that can otherwise degrade the BANN accuracy. Our approach outperforms existing BNNs, SNNs, and adder neural networks (that also avoid energy-expensive multiplication operations similar to BNNs and SNNs) in terms of the accuracy-FLOPs trade-off for complex image recognition tasks. Downstream experiments on object detection further demonstrate the efficacy of our approach. Lastly, we demonstrate the portability of our approach to SNNs with multiple time steps. Codes are publicly available here.

1 Introduction

Due to its low memory footprint and use of cheaper pop-count operations instead of energy-expensive multiply-and-accumulates (MAC), BNNs have emerged as a promising low-power alternative to compute- and memory-expensive deep neural networks (DNN) (Rastegari et al., 2016; Liu et al., 2020a; 2018a). Recent works have proposed novel network architectures (Bethge et al., 2021; Zhang et al., 2022; Shi et al., 2022; Hu et al., 2022) and training algorithms (Zhijun Tu & Wang, 2022a; Xu et al., 2021b; Rastegari et al., 2016; Bulat & Tzimiropoulos, 2019; Geng et al., 2023; Chen et al., 2021; Xu et al., 2021a; Kim et al., 2021; Wang et al., 2023; Lee et al., 2022) to approximate the full-precision representation of the weights and activations with 1-bit bi-polar values without significant drop in accuracy.

However, most of these efforts induce a significant number of non-binary operations which degrade the computational efficiency. For example, ReactNet-based BNNs (Liu et al., 2020a; Zhijun Tu & Wang, 2022b) incur custom non-linear functions, including RPReLU that are significantly more complex compared to threshold or ReLU operations, duplicated basic blocks that significantly increase the total number of floating point operations (FLOPs) and parameter count. Moreover, all these BNNs employ the *sign* quantization function to generate the bi-polar weights and activation values. However, bi-polar activations do not yield any sparsity and thus can not benefit any computational efficiency from hardware that can leverage sparsity. Moreover, as shown in (Wang et al., 2020b; Lin et al., 2023; Falkena et al., 2023), it is also unclear whether *sign* is the optimal binarization function.

In contrast, SNNs can provide significant sparsity, even up to 80% for ultra-low number of time steps (Chowdhury et al., 2021). However, this comes at the cost of significant accuracy drop (Datta et al., 2021) without any specialized neuron model (Datta et al., 2023b). In an attempt to push the frontier of sparsity-accuracy trade-off, we propose a class of uni-polar binary activation neural networks (BANNs) that can enjoy sparsity similar to SNNs while getting rid of the temporal dimension, and achieve BNN-like accuracies. Our BANNs are more compute-efficient than existing bi-polar BNNs. This efficiency stems from the fact that we can skip the memory access of the weight and the eventual accumulate/bit-count operation when the corresponding activation value is 0.

Our Contributions. Our training framework for BANNs is based on a novel application of the Hoyer regularizer and a novel Hoyer thresholding layer. More specifically, our threshold is training-input-dependent and is set to be equal to the Hoyer extremum of a clipped version of the activation tensor, where the clipping value is trained using gradient descent with our Hoyer regularizer. In this way, compared to traditional uni-polar BNNs and SNNs with ultra-low number of time steps, our threshold increases the rate of weight updates and our Hoyer regularizer shifts the activation distribution away from this threshold, improving convergence. We consistently surpass the accuracies obtained by SOTA uni-polar BNNs (Wang et al., 2020b; Sakr et al., 2018) on diverse image recognition datasets with different convolutional architectures. Compared to SNNs, and adder neural network (AddNN) models that are also compute-efficient, our BANN models yield higher test accuracy with a $\sim 5.5\times$ reduction in floating point operations (FLOPs), thanks to the extreme sparsity enabled by our training framework. Incorporating the training framework of BANNs can also improve the test accuracy in advanced bi-polar BNNs. Downstream tasks on object detection also demonstrate that our approach surpasses the test mAP of existing BNNs and SNNs. Our approach can also be incorporated to SNNs with multiple time steps, thereby leading to small but significant accuracy increase at the cost of significant increase in memory and compute cost. Thus, *our proposed approach acts as a continuum between one time-step sparse BNNs and low time-step SNNs, and can help bridge both the BNN and SNN communities for low-power vision tasks.*

2 PRELIMINARIES

2.1 HOYER REGULARIZER

Based on the interplay between ℓ_1 and ℓ_2 norms, a new measure of sparsity was first introduced in (Hoyer, 2004), based on which, (Yang et al., 2020) proposed a new regularizer, termed the Hoyer regularizer for the trainable weights that was incorporated into the loss term to train DNNs. We adopt the same form of Hoyer regularizer for the activation to train our BANN models as $H(\boldsymbol{u}_l) = \left(\frac{\|\boldsymbol{u}_l\|_1}{\|\boldsymbol{u}_l\|_2}\right)^2$ (Kurtz et al., 2020). Here, $\|\boldsymbol{u}_l\|_i$ represents the ℓ_i norm of the activation tensor $\boldsymbol{u}_l$, and the superscript t for the time step is omitted for simplicity. Compared to the ℓ_1 and ℓ_2 regularizers, the Hoyer regularizer has scale-invariance (similar to the ℓ_0 regularizer). It is also differentiable almost everywhere (see equation 1) where $|\boldsymbol{u}_l|$ represents the element-wise absolute of the tensor $\boldsymbol{u}_l$.

$$\frac{\partial H(\boldsymbol{u}_l)}{\partial \boldsymbol{u}_l} = \frac{2\|\boldsymbol{u}_l\|_1}{\|\boldsymbol{u}_l\|_2^2}\left(sign(\boldsymbol{u}_l)\cdot\|\boldsymbol{u}_l\|_2 - \frac{\|\boldsymbol{u}_l\|_1}{\|\boldsymbol{u}_l\|_2}\boldsymbol{u}_l\right) \tag{1}$$

Letting the gradient $\frac{\partial H(\boldsymbol{u}_l)}{\partial u_l}=0$ and making all the $\boldsymbol{u}_l$ positive, the value of the Hoyer extremum becomes $E(\boldsymbol{u}_l)=\frac{\|\boldsymbol{u}_l\|_2^2}{\|\boldsymbol{u}_l\|_1}$. This extremum is the minimum, because the second derivative is greater than zero for any value of the output element. Training with the Hoyer regularizer can effectively help push the activation values that are larger than the extremum ($\boldsymbol{u}_l > E(\boldsymbol{u}_l)$) even larger and those that are smaller than the extremum ($\boldsymbol{u}_l < E(\boldsymbol{u}_l)$) even smaller.

2.2 Binary Neural Networks

Given a input $\boldsymbol{o}_{l-1} \in \mathbb{R}^{c \times h \times w}$ and weight $\boldsymbol{w} \in \mathbb{R}^{n \times c \times k \times k}$ of a layer l, we can get the output $\boldsymbol{u}_l \in \mathbb{R}^{c \times h' \times w'}$ by convolution operation as $\boldsymbol{u}_l = \boldsymbol{o}_{l-1} * \boldsymbol{w}_l$. To accelerate the inference process, bi-polar BNNs (Liu et al., 2020a; Zhijun Tu & Wang, 2022b) partition the input and weight into two clusters, -1 and +1 with sign function as Eq. 2.

$$sign(x) = \begin{cases} 1, & \text{if } x \geq 0; \\ -1, & \text{otherwise} \end{cases} \tag{2}$$

To yield sparsity similar to ReLU activation, uni-polar BNNs (Wang et al., 2020b; Sakr et al., 2018) parition the weights to -1 and +1, while the activations to 0 and 1 as illustrated below in Eq. 3.

$$\boldsymbol{z}_l = \frac{\boldsymbol{u}_l}{v_l^{th}} \qquad \boldsymbol{o}_l = \begin{cases} 1, & \text{if } \boldsymbol{z}_l \geq 1; \\ 0, & \text{otherwise} \end{cases} \tag{3}$$

where $\boldsymbol{z}_l$ denotes the normalized activation output, and v_l^{th} denotes a trainable threshold parameter. While our BANNs primarily focus on sparse uni-polar activations with full-precision weights (activations are significantly more difficult to binarize compared to weights (Lin et al., 2017b; Ding et al., 2019)), we also demonstrate the efficacy of BANNs with binary weights (-1 and +1) for a fair comparison with BNNs.

3 Proposed Training Framework

Our approach is inspired by the fact that Hoyer regularizers can shift the pre-activation distributions away from the Hoyer extremum in a DNN (Yang et al., 2020). Our principal insight is that setting our activation threshold to this extremum shifts the distribution away from the threshold value, reducing noise and improving convergence. To obtain our BANNs, we present a novel *Hoyer threshold layer* that sets the threshold based upon a *Hoyer regularized training process*, as described below.

3.1 Hoyer threshold layer

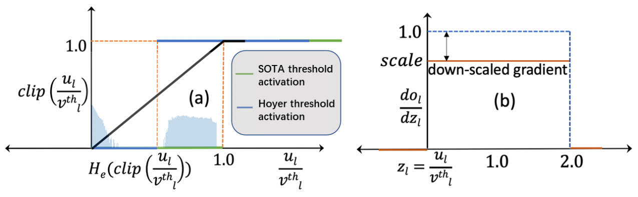

Figure 1: (a) Comparison of our Hoyer threshold function with existing uni-polar binary activation functions where the blue distribution denotes the shifting of pre-activation values away from the threshold using Hoyer regularized training, (b) Proposed derivative of our Hoyer threshold function.

As illustrated above in Eq. 3, a binary neuron with a unit step activation function is difficult to optimize with straight through estimator (STE) based approaches (Bengio et al., 2013), which either approximates the binary neuron functionality with a continuous differentiable model or surrogate gradient approaches used in SNNs (Panda & Roy, 2016; Lee et al., 2016). This is because the number of *ones* in the activations becomes too low to adjust the weights sufficiently using gradient descent. If a pre-synaptic neuron does not output 1, the synaptic weight connected to it cannot be updated because its gradient from neuron i is calculated as $g_{u_j} \times o_i$, where g_{u_j} is the gradient of the activation u_j and o_i is the output of neuron i.

Therefore, it is crucial to reduce the value of the threshold to generate enough 1s for better network convergence. However, a sufficiently low value of threshold can generate a *one* for every neuron, but that would yield random outputs in the final classifier layer. Hence, it is challenging to yield the optimal threshold for each layer. Previous works (Wang et al., 2020b) show that this problem can be partially mitigating by training the threshold term v_l^{th} using gradient descent. However, that still leads to a large accuracy gap with the SOTA bi-polar BNNs, especially for ImageNet-level tasks.

In contrast, we propose to dynamically down-scale the threshold (see Fig. 1(a)) based on the activation using our proposed form of the Hoyer regularizer. In particular, we clip the activation corresponding to each convolutional layer to the trainable threshold v_l^{th} obtained from the gradient descent with our Hoyer loss, as detailed later in Eq. 12. Unlike existing approaches (Rathi et al., 2020a; Chowdhury et al., 2021) that require v_l^{th} to be initialized from a pre-trained full-precision model, our approach can be used to train BANNs from scratch with a Kaiming uniform initialization (He et al., 2015) for both the weights and thresholds. In particular, the normalized down-scaled threshold value, with which we compare the normalized activation z_l, for each layer is computed as the Hoyer extremum of the clipped activation tensor as shown in Fig. 1(a) and below.

$$\boldsymbol{z}_l^{clip} = \begin{cases} 1, \text{if } \boldsymbol{z}_l > 1 \\ \boldsymbol{z}_l, \text{if } 0 \le \boldsymbol{z}_l \le 1 \\ 0, \text{if } \boldsymbol{z}_l < 0 \end{cases} \quad \boldsymbol{o}_l = h_s(\boldsymbol{z}_l) = \begin{cases} 1, \text{if } \boldsymbol{z}_l \ge E(\boldsymbol{z}_l^{clip}) \\ 0, \text{otherwise} \end{cases} \tag{4}$$

Note that our normalized threshold $E(\boldsymbol{z}_l^{clip})$ is less than the normalized threshold whose value is 1 for any output (proof in supplementary materials). Hence, our actual threshold value $E(\boldsymbol{z}_l^{clip}) \times v_l^{th}$ is indeed less than the trainable threshold v_l^{th} used in earlier works (Datta & Beerel, 2022; Rathi et al., 2020a). We also observe that the Hoyer extremum in each layer changes only slightly during the later stages of training, which indicates that it is most likely an inherent attribute of the dataset and model architecture. Hence, to estimate the threshold during inference, we calculate the exponential average of the Hoyer extremums during training, similar to batch normalization (BN) layers, and use the same during inference.

3.2 Hoyer Regularized Training

The loss function (L_{total}) of our proposed approach is shown below in Eq. 5.

$$L_{total} = L_{CE} + \lambda_H L_H = L_{CE} + \lambda_H \sum_{l=1}^{L-1} H(\boldsymbol{z}_l^{clip}) \tag{5}$$

where L_{CE} denotes the cross-entropy loss calculated on the softmax output of the last layer L, and L_H represents the Hoyer regularizer calculated on the input of our Hoyer threshold layer after dividing the threshold term v_l^{th} and clipping. The weight update for the layer $L-1$ is computed as

$$\begin{aligned} \Delta W_{L-1} &= \frac{\partial L_{CE}}{\partial \boldsymbol{w}_{L-1}} + \lambda_H \frac{\partial L_H}{\partial \boldsymbol{w}_{L-1}} = \frac{\partial L_{CE}}{\partial \boldsymbol{o}_{L-1}} \frac{\partial \boldsymbol{o}_{L-1}}{\partial \boldsymbol{u}_{L-1}} \frac{\partial \boldsymbol{u}_{L-1}}{\partial \boldsymbol{w}_{L-1}} + \lambda_H \frac{\partial L_H}{\partial \boldsymbol{u}_{L-1}} \frac{\partial \boldsymbol{u}_{L-1}}{\partial \boldsymbol{w}_{L-1}} \\ &= \left(\frac{\partial L_{CE}}{\partial \boldsymbol{o}_{L-1}} \frac{\partial \boldsymbol{o}_{L-1}}{\partial \boldsymbol{u}_{L-1}} + \lambda_H \frac{\partial H(\boldsymbol{z}_{L-1}^{clip})}{\partial \boldsymbol{u}_{L-1}} \right) \boldsymbol{o}_{L-2} \end{aligned} \tag{6}$$

$$\frac{\partial L_{CE}}{\partial \boldsymbol{o}_{L-1}} = \frac{\partial L_{CE}}{\partial \boldsymbol{u}_L} \frac{\partial \boldsymbol{u}_L}{\partial \boldsymbol{o}_{L-1}} = (\boldsymbol{s} - \boldsymbol{y}) \boldsymbol{w}_L \tag{7}$$

where $\boldsymbol{s}$ denotes the output softmax tensor, i.e., $s_i = \frac{e^{u_L^i}}{\sum_{k=1}^{N} u_L^k}$ where u_L^i and u_L^k denote the i^{th} and k^{th} elements of the activation tensor of the last layer L, and N denotes the number of classes. Note that $\boldsymbol{y}$ denotes the one-hot encoded tensor of the true label, and $\frac{\partial H(\boldsymbol{u}_L)}{\partial \boldsymbol{u}_L}$ is computed using Eq. 1. The last layer does not have any threshold and yields full-precision outputs.

The weight and threshold update computations for the hidden layers are in Appendix A.1.

Note that all the derivatives to update the trainable parameters can be computed by Pytorch autograd, except the derivative $\frac{\partial \boldsymbol{o}_l}{\partial \boldsymbol{z}_l}$, whose gradient is zero almost everywhere and undefined at z_l=0. We extend the existing idea of surrogate gradient descent (SGD) (Neftci et al., 2019) in SNNs to compute this derivative for our BANNs with Hoyer threshold layers, as illustrated in Fig. 1(b) and mathematically defined as follows.

$$\frac{\partial \boldsymbol{o}_l}{\partial \boldsymbol{z}_l} = \begin{cases} \textit{scale} \times 1 & \text{if } 0 < \boldsymbol{z}_l < 2 \\ 0 & \text{otherwise} \end{cases} \tag{8}$$

where *scale* denotes a hyperparameter that controls the dampening of the gradient. Note that o_l jumps from 0 to 1 at z_l=1. We assume the surrogate gradient is non-zero spanning a width of 1 in both directions around z_l=1.

Table 1: Comparison of the test accuracy of our BANNs with full-precision DNNs for object recognition. Model* indicates that we remove the first max pooling layer, and Sp. denotes sparsity.

Network	dataset	DNN (%)	BANN (%)	Sp. (%)
VGG16	CIFAR10	94.10	93.44	78.13
ResNet18	CIFAR10	93.34	92.50	74.17
ResNet18*	CIFAR10	94.28	93.88	83.88
ResNet20	CIFAR10	93.18	92.39	76.31
ResNet34*	CIFAR10	94.68	93.53	83.96
ResNet50*	CIFAR10	94.90	94.07	82.21
VGG16	ImageNet	70.08	68.00	75.52
ResNet50	ImageNet	73.12	66.98	76.11

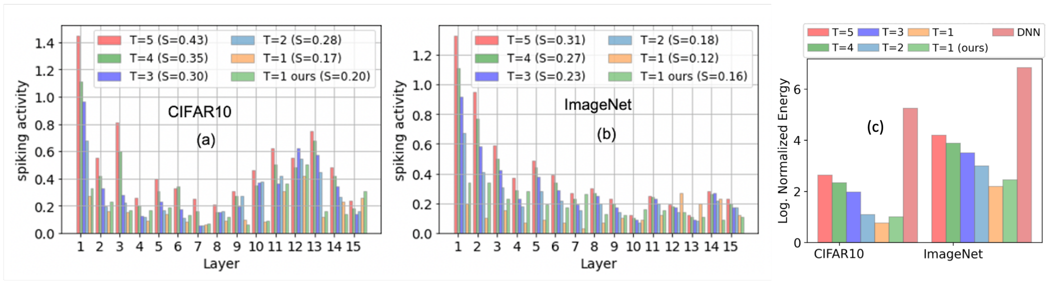

Figure 2: Layerwise spiking activities for a VGG16 across time steps ranging from 5 to 1 (average spiking activity denoted as S in parenthesis) representing existing low-latency SNNs including our work (which represents one time step) on (a) CIFAR10, (b) ImageNet, (c) Comparison of the total energy consumption between SNNs with different time steps and full-precision DNNs.

4 Experimental Results

Datasets & Models: Similar to existing BNN and SNN works (Rathi et al., 2020b;a; Liu et al., 2020a), we perform object recognition experiments on CIFAR10 (Krizhevsky, 2009) and ImageNet (Deng et al., 2009) dataset using VGG16 (Simonyan & Zisserman, 2014) and several variants of ResNet (He et al., 2016) architectures. For object detection, we use the MMDetection framework (Chen et al., 2019) with PASCAL VOC2007 and VOC2014 (Everingham et al., 2010) as training dataset, and benchmark our BANN models and the baselines on the VOC2007 test dataset. We use the Faster R-CNN (Ren et al., 2015) and RetinaNet (Lin et al., 2017a) framework, and substitute the original backbone with our BANN models pretrained on ImageNet.

Object Recognition Results: For training the recognition models, we use the Adam (Kingma & Ba, 2014) optimizer for VGG16, and use SGD optimizer for ResNet models. As shown in Table 1 with FP weights, we obtain the SOTA accuracy of 93.44% on CIFAR10 with VGG16; the accuracy of our ResNet-based BANNs on ImageNet also surpasses the existing works. Note that our ResNet models are based on the spike-element-wise (SEW) architecture (Fang et al., 2020) as detailed in Appendix A.2. On ImageNet, we obtain a 68.00% top-1 accuracy with VGG16 which is only $\sim$2% lower compared to the iso-architecture full-precision counterpart. All our BANN models yield a sparsity of $\sim$75% or higher on both CIFAR10 and ImageNet, which is significantly higher compared to existing SNNs/BNNs as shown in Fig. 2.

Accuracy Comparison with SNNs: We compare our results with various SOTA ultra low-latency SNNs for image recognition tasks in Table 2. Our BANNs yield comparable or better test accuracy compared to all the existing works on both CIFAR10 and ImageNet, with significantly lower inference latency (due to the existence of multiple time steps in SOTA SNNs). The only exception for the latency reduction is the one-time-step SNN proposed in (Chowdhury et al., 2021), however, it increases the training time significantly as illustrated later in Fig. 3.

Energy Efficiency Comparison with SNNs and full-precision DNNs: We compare the energy-efficiency of our BANNs with full-precision DNNs and existing multi-time-step SNNs in Fig. 2. The compute-efficiency of BANNs stems from two factors: 1) sparsity, that reduces the number of synaptic operations in convolutional and linear layers compared to full-precision DNNs according to $\text{SNN}_l^{flops} = S_l \times \text{DNN}_l^{flops}$ (Chowdhury et al., 2021), where S_l denotes the average number of spikes per neuron per inference over all timesteps in layer l. Note that the sparsity induces a small

Table 2: Comparison of our BANN models to existing SNNs. SGD and hybrid denote surrogate gradient descent and pre-trained DNN followed by SNN fine-tuning respectively. (qC, dL) denotes an architecture with q convolutional and d linear layers. T.S denotes the number of time steps. *Results reported without autoaugmentation and cutout for fair comparison with our work.

Ref.	Training	Architecture	Acc. (%)	T.S
Dataset : CIFAR10				
(Meng et al., 2022)	SGD	PreAct-ResNet19	**95.40**	20
(Deng et al., 2021)	DNN-SNN conversion	VGG16	92.29	16
(Bu et al., 2022a)	DNN-SNN cooversion	VGG16	90.96	8
(Zhang & Li, 2020)	SGD	5C, 2L	91.41	5
(Rathi et al., 2020a)	Hybrid	VGG16	92.70	5
(Zheng et al., 2021)	STBP-tdBN	ResNet19	93.16	6
(Datta & Beerel, 2022)	Hybrid	VGG16	91.79	2
(Bu et al., 2022b)	DNN-SNN conversion	VGG16	91.18	2
(Fang et al., 2020)	SGD	5C, 2L	93.50	8
(Deng et al., 2023)*	SGD	ResNet18	**94.58**	2
(Xiao et al., 2022)	SGD	VGG (sWS)	93.73	6
(Deng et al., 2022)	SGD	ResNet19	94.16	2
(Li et al., 2021b)	SGD	ResNet18	93.13	2
(Chowdhury et al., 2021)	Hybrid	VGG16	93.05	1
(Chowdhury et al., 2021)	Hybrid	ResNet20	91.10	1
Ours	**Adam+Hoyer Reg.**	**VGG16**	**93.44**	**1**
Dataset : ImageNet				
(Bu et al., 2022b)	DNN-SNN conversion	ResNet34	59.35	16
(Li et al., 2021b)	SGD	ResNet18	**71.24**	5
(Rathi et al., 2020a)	Hybrid	VGG16	69.00	5
(Fang et al., 2021)	SGD	ResNet34	67.04	4
(Fang et al., 2021)	SGD	ResNet152	**69.26**	4
(Deng et al., 2023)*	SGD	ResNet34	65.77	2
(Duan et al., 2022)	SGD	ResNet34	68.28	4
(Deng et al., 2022)	SGD	ResNet19	68.00	4
(Rathi et al., 2020a)	Hybrid	VGG16	69.00	5
(Zheng et al., 2021)	STBP-tdBN	ResNet34	67.05	6
(Chowdhury et al., 2021)	Hybrid	VGG16	67.71	1
Ours	**Adam+Hoyer Reg.**	**VGG16**	**68.00**	**1**

overhead of checking whether the 1-bit activation is zero, which consumes 0.05pJ in 28nm Kintex-7 FPGA platform according to our post place-and-route simulations. 2) Use of only AC (1.8pJ) operations that consume 7.4$\times$ lower compared to each MAC (13.32pJ) operation in our FPGA setup for floating point (FP) representation. Note that the binary activations can replace the FP multiplications with logical operations, i.e., conditional assignment to 0 with a bank of AND gates. These replacements may be realized using existing hardware depending on the compiler and the details of their data paths. Building a custom accelerator that can efficiently implement these reduced operations is also possible (Wang et al., 2020a; Frenkel et al., 2019; Lee & Li, 2020). Additionally, our BANNs also enjoy superior memory-efficiency compared to existing multi-time-step SNNs since the latter requires the membrane potentials and weights to be fetched from and read to the on-/off-chip memory for each time step. Our BANNs can avoid these repetitive read/write operations as it does involve any *state* and lead to a $T\times$ reduction in the number of memory accesses compared to a T-time-step SNN model. Compared to traditional bi-polar BNNs, our BANNs can also reduce the number of memory accesses with the support of zero gating logic leveraging the high activation sparsity. This can be achieved by skipping the reading of the weights when the activation associated to it is zero. However, the exact savings in memory energy will depend on the weight reuse scheme and the underlying hardware. We have provided the detailed energy model of traditional BNNs, multi-time-step SNNs, BANNs, and full-precision DNNs, considering the sparsity overhead and memory accesses without any weight reuse scheme, in Appendix A.9. We compare the layer-wise spiking activities S_l for time steps ranging from 5 to 1 in Fig. 2(a-b) that are computed based on the

Table 3: Accuracies from different strategies to train BANNs on CIFAR10

Training Strategies	Pretrained DNN(%)	BANN (%)	Sparsity (%)
Pre-trained+fine-tuning	93.15	91.39	23.56
Iterative training (N=10)	93.25	92.68	10.22
Iterative Training (N=20)	92.68	92.24	9.54
Proposed Training	-	**93.13**	22.57

Table 4: Accuracies and energies of weight quantized BANN models based on VGG16 on CIFAR10 where FP is 32-bit floating point.

Dataset	Bits	Acc. (%)	Spiking Activity (%)	Energy (mJ)
CIFAR10	FP	93.44	22.57	18.67
CIFAR10	6	93.11	22.46	7.46
CIFAR10	2	92.94	21.39	5.66
CIFAR10	1	92.80	22.68	5.02
ImageNet	FP	68.00	24.48	424.3
ImageNet	2	66.86	23.82	231.3
ImageNet	1	64.62	23.99	221.8

replicated implementation of an existing low-latency SNN (Rathi et al., 2020a), against our work (where the spiking activity denotes the number of 1s) that represents a time step of 1. Note, the spike rates decrease significantly with time step reduction from 5 to 1, leading to considerably lower FLOPs in our one-time-step SNNs. These lower FLOPs, coupled with the $7.4\times$ reduction for AC operations and the sparsity overhead, lead to a $22.7\times$ and $31.9\times$ reduction in compute energy on CIFAR10 and ImageNet respectively with VGG16. Considering the memory accesses as provided in our energy models in A.9, the total energy reduces by $70.28\times$ and $81.13\times$.

Comparison with different training strategies: Based on existing BNN and SNN literature, we hypothesize that two training strategies that can be effectively used to train BANNs, other than our proposed approach.

Pre-trained DNN, followed by BANN fine-tuning. Similar to the hybrid training proposed in (Rathi et al., 2020b), we pre-train a full-precision DNN model, and copy its weights to the BANN model. Initialized with these weights, we train our BANN with normal cross-entropy loss.

Iteratively convert ReLU neurons to binary neurons. First, we train a DNN model which uses the ReLU activation with threshold, then we iteratively reduce the number of the ReLU neurons whose output activations are multi-bit. Specifically, we first force the activation values in the top N percentile to output 1, and those in bottom N percentile percent to output 0, and gradually increase N until the accuracy drops beyond a certain threshold or all neuron outputs are either 1 or 0.

Proposed training from scratch. With our proposed Hoyer threshold layer and Hoyer regularized training, we train a BANN model from scratch. Our results with these training strategies are shown in Table 3, which indicates that it is difficult for training strategies that involve pre-training and fine-tuning to approach the accuracy of full-precision models with BANNs. One possible reason for this might be the difference in the distribution of the pre-activation values between the DNN and BANN models (Datta & Beerel, 2022). Our Hoyer threshold layer and our Hoyer regularizer, can help train a BANN model with SOTA accuracy from scratch.

Effect on Quantization: In order to further improve the energy efficiency of our BANNs, we perform quantization-aware training of the weights in our models to $1-6$ bits for both CIFAR10 and ImageNet. This transforms the FP ACs to $1-6$ bit ACs, thereby leading to a $4.8-13.8$ reduction in compute energy as obtained from our FPGA simulations. The reduced weight precision also reduces the memory access cost by $\sim 5-32\times$ with efficient bit-packing (bit, 2021) for $1-6$ bits according to our FPGA simulations. Note that we only quantize the convolutional layers, as quantizing the linear layers lead to a noticeable drop in accuracy. As shown in Table 4, when quantized to 6 bits, our VGG-based BANN incur a negligible accuracy drop of only 0.02% on CIFAR10, while reducing the total energy by $3.3\times$ (energy computed from the models developed in A.9). Even with 1-bit quantization, our model can yield an accuracy of 92.80% without any special modification, while still yielding a sparsity of $\sim 78\%$.

Comparison with AddNNs & BNNs: We compare the accuracy and energy of our BANN

Table 5: Accuracy & Energy Comparison of our BANNs to AddNNs and BNNs

Reference	Dataset	Acc.(%)	Energy (mJ)
Uni-polar BNNs			
(Sakr et al., 2018)	CIFAR10	89.6	4.94
(Wang et al., 2020b)	ImageNet	59.7	215.0
Bi-polar BNNs			
(Diffenderfer & Kailkhura, 2021)	CIFAR10	91.9	14.72
AddNNs			
(Chen et al., 2020) (FP weights)	CIFAR10	93.72	95.22
(Chen et al., 2020) (2-bit weights)	CIFAR10	92.08	24.57
(Chen et al., 2020) (FP weights)	ImageNet	67.0	2291.2
Our BANNs			
This work (FP weights)	CIFAR10	93.44	18.67
This work (1-bit weights)	CIFAR10	92.80	5.02
This work (FP weights)	ImageNet	68.00	424.3
This work (1-bit weights)	ImageNet	64.62	221.8

Table 7: Test accuracy obtained by our approach with multiple time steps for SNNs on CIFAR10.

Architecture	Time steps	Acc. (%)	Spiking activity (%)
VGG16	1	93.44	21.87
VGG16	2	93.71	44.06
VGG16	6	94.14	101.22
ResNet18	1	91.48	25.83
RseNet18	2	91.93	33.24
ResNet18	6	92.01	83.82

models with recently proposed AddNN models (Chen et al., 2020) that also removes multiplications for increased energy-efficiency in Table 5. With the VGG16 architecture, on CIFAR10, we obtain 0.6% lower accuracy, while on ImageNet, we obtain 1.0% higher accuracy. Moreover, unlike our BANNs and SNNs, AddNNs do not yield any sparsity, and consume $\sim 5.1\times$ more compute energy (with the sparsity overhead incorporated) compared to our BANNs on average across both CIFAR10 and ImageNet (see Table 5). We also compare our BANN models with SOTA BNNs in Table 7 that replaces the costly MAC operations with cheaper pop-count counterparts, thanks to the binary weights and activations. Our BANNs with 2-bit quantized weights consume $2.6\times$ lower energy compared to the bi-polar BNNs (see (Diffenderfer & Kailkhura, 2021) in Table 5). This is due to the improved trade-off between the high sparsity activity ($\sim 78\%$ as shown in Table 1) provided by our BANN models, and less energy due to XOR operations and 1-bit memory access compared to weight-quantized ACs and 2-bit memory access. On the other hand, our BANNs with 1-bit weights i.e., our sparse uni-polar BNNs consume similar energy compared to existing unipolar BNNs (see (Sakr et al., 2018; Wang et al., 2020b) in Table 5) while yielding 2.6% higher accuracy (92.80% vs 90.2%) on CIFAR10 and 4.9% higher accuracy (64.62% vs 59.7%) on ImageNet at iso-architecture. Lastly, it is worth mentioning that though our sparse BNNs can surpass test accuracies obtained by a few existing BNNs, it fails to yield accuracies similar to the SOTA bi-polar BNNs (Zhang et al., 2022; Bethge et al., 2021; Zhijun Tu & Wang, 2022a; Xu et al., 2021b). This is due to their higher expressivity (further explained in A.11) and network modifications (e.g. ReactNet with PReLU compared to our simple VGG and ResNets) that increases the FLOPs by more than $2\times$. However, applying our proposed training technique on these BNNs results in

Table 6: Impact of our proposed Hoyer regularized training framework on the test accuracy with advanced BNNs

Work	Acc. (%)	Acc. w/ Hoyer (%)
PokeBNN-1.0x	73.4	73.6 (+0.2)
MeliusNet59	71.0	72.3 (+1.3)
ReCU (Resnet18)	66.4	67.8 (+1.4)

$0.2-1.3\%$ increase in test accuracy as shown in Table 6. This is done using the same way as using the Hoyer extremum of the normalized and clipped activation as the threshold, where the clipping is done at -1 and +1 (instead of 0 and +1 for our BANNs). This demonstrate the efficacy of our proposed method.

Extension to SNNs: We extend our proposed approach to multi-time-step SNN models by adopting the standard LIF model (Sengupta et al., 2019) for the neurons but computing the threshold based on the Hoyer extremum defined in Eq. 3 and unrolling the gradients derived in Section 3.2 using traditional backpropagation through time (Rathi et al., 2020a). As shown in Table 7, as time step increases from 1 to 6, the accuracy of our model also increases from 93.44% to 94.14%, which validates the effectiveness of our method. However, this accuracy increases comes at the cost of a significant increase in spiking activity (see Table 7 where the spiking activity is computed across the total number of time steps similar to (Sengupta et al., 2019)), increasing the compute energy. The memory cost also increases due to the repetitive potential and weight accesses across time steps.

5 Relationship between SNN, BNN, and BANN

Our BANNs are identical to uni-polar sparse BNNs (Sakr et al., 2018; Wang et al., 2020b) when the weight precision is quantized down to 1-bit. Our BANNs are also identical to one-time-step SNNs, and can be readily extended to traditional multi-time-step SNNs with the incorporation of the membrane potential, using the traditional LIF model for the neurons where the membrane potential integrates the weight modulated input spikes and leaks over time. We use the soft reset mechanism that reduces the membrane potential by the threshold value when an output spike generated (Datta et al., 2023a). It has been shown that soft reset minimizes the information loss by allowing the spiking neuron to carry forward the surplus potential above the firing threshold to the subsequent time step (). We use our proposed combination of Hoyer regularized training and Hoyer spike layer to train the per layer threshold, while we train the weights and leak term using SGL. The dynamics of our LIF model for our multi-time-step SNNs are shown below.

$U_i^{mp}(t)=\lambda U_i(t-1)+\sum_j W_{ij}S_j(t), \quad S_i(t)=1 \text{ if } U_i^{mp}(t)>V^{th} \text{ else } 0, \quad U_i(t)=U_i^{mp}(t)-S_i(t)V^{th}$

Here $U_i(t)$ denotes the membrane potential of the i^{th} neuron at timer step t, $S_i(t)$ denotes the binary output of the i^{th} neuron at time step t, V^{th} denotes the threshold, λ denotes the leak, and W_{ij} denotes the weight connecting the pre-synaptic neuron j and the neuron i.

The sparse activation in BANNs bears resemblance to SNNs while the difference is that there is no temporal dimension. On the other hand, the 1-bit sparse activation in BANNs bears resemblance to BNNs, in particular uni-polar BNNs, while the difference is that the weight precision is multi-bit. Thus, BANNs can bridge the gap between BNNs and SNNs by bringing the activation sparsity of SNNs to BNNs, and removing the temporal dimension of SNNs for equivalence with BNNs.

6 Conclusions

In this work, we propose BANNs trained using a novel variant of Hoyer Regularizer and a Hoyer threshold layer that jointly optimizes the distribution of the BANN pre-activations and the placement of the BANN threshold in order to improve the accuracy-FLOPs trade-off compared to existing networks. Our Hoyer regularizer introduces a loss term that penalizes the normalized and clipped activation values around their Hoyer extremum (which depends on the SGD trained threshold). Our proposed Hoyer threshold layer takes advantage of this distribution shift by setting the IF threshold to the Hoyer extremum. Our BANN models surpass test accuracies obtained by existing SNN, uni-polar BNN, and AddNN models with similar or better energy-efficiency. Our training framework can also improve the accuracy of a number of advanced bi-polar BNNs. Our SNNs can further improve the inference energy and latency efficiency with recently proposed in-sensor computing systems (Datta et al., 2022d;a;c) where the bandwidth between the sensor that implements the first few CNN layers and the back-end processing unit that implements the remaining layers can be significantly reduced, thanks to the binary activations for only one time step (Datta et al., 2023c).

7 Acknowledgement

This work is supported by a gift funding from Intel Labs.

REFERENCES

Bit-Packing Compressor in FPGA-Hardware. https://textarossa.eu/bit-packing-compressor-in-fpga-hardware/, 2021.

Yoshua Bengio, Nicholas Léonard, and Aaron Courville. Estimating or propagating gradients through stochastic neurons for conditional computation. *arXiv preprint arXiv:1308.3432*, 2013.

Joseph Bethge, Christian Bartz, Haojin Yang, Ying Chen, and Christoph Meinel. Meliusnet: An improved network architecture for binary neural networks. In *2021 IEEE Winter Conference on Applications of Computer Vision (WACV)*, pp. 1438–1447, 2021. doi: 10.1109/WACV48630.2021.00148.

Tong Bu, Jianhao Ding, Zhaofei Yu, and Tiejun Huang. Optimized potential initialization for low-latency spiking neural networks. *Proceedings of the AAAI Conference on Artificial Intelligence*, 36(1):11–20, Jun. 2022a. doi: 10.1609/aaai.v36i1.19874. URL https://ojs.aaai.org/index.php/AAAI/article/view/19874.

Tong Bu, Wei Fang, Jianhao Ding, PENGLIN DAI, Zhaofei Yu, and Tiejun Huang. Optimal ANN-SNN conversion for high-accuracy and ultra-low-latency spiking neural networks. In *International Conference on Learning Representations*, 2022b. URL https://openreview.net/forum?id=7B3IJMM1k_M.

Adrian Bulat and Georgios Tzimiropoulos. Xnor-net++: Improved binary neural networks, 2019.

Hanting Chen, Yunhe Wang, Chunjing Xu, Boxin Shi, Chao Xu, Qi Tian, and Chang Xu. Addernet: Do we really need multiplications in deep learning? In *Proceedings of the IEEE/CVF Conference on Computer Vision and Pattern Recognition (CVPR)*, June 2020.

Kai Chen, Jiaqi Wang, Jiangmiao Pang, Yuhang Cao, Yu Xiong, Xiaoxiao Li, Shuyang Sun, Wansen Feng, Ziwei Liu, Jiarui Xu, Zheng Zhang, Dazhi Cheng, Chenchen Zhu, Tianheng Cheng, Qijie Zhao, Buyu Li, Xin Lu, Rui Zhu, Yue Wu, Jifeng Dai, Jingdong Wang, Jianping Shi, Wanli Ouyang, Chen Change Loy, and Dahua Lin. MMDetection: Open MMLab detection toolbox and benchmark. *arXiv preprint arXiv:1906.07155*, 2019.

Tianlong Chen, Zhenyu Zhang, Xu Ouyang, Zechun Liu, Zhiqiang Shen, and Zhangyang Wang. ”bnn - bn = ?”: Training binary neural networks without batch normalization. In *Proceedings of the IEEE/CVF Conference on Computer Vision and Pattern Recognition (CVPR) Workshops*, pp. 4619–4629, June 2021.

Sayeed Shafayet Chowdhury et al. One timestep is all you need: Training spiking neural networks with ultra low latency. *arXiv preprint arXiv:2110.05929*, 2021.

G. Datta, S. Kundu, Z. Yin, R. T. Lakkireddy, J. Mathai, A. P. Jacob, P. A. Beerel, and A. R. Jaiswal. A processing-in-pixel-in-memory paradigm for resource-constrained tinyml applications. *Scientific Reports*, 12, 2022a. URL https://doi.org/10.1038/s41598-022-17934-1.

Gourav Datta and Peter A. Beerel. Can deep neural networks be converted to ultra low-latency spiking neural networks? In *2022 Design, Automation & Test in Europe Conference & Exhibition (DATE)*, volume 1, pp. 718–723, 2022. doi: 10.23919/DATE54114.2022.9774704.

Gourav Datta, Souvik Kundu, Akhilesh R. Jaiswal, and Peter A. Beerel. ACE-SNN: Algorithm-Hardware co-design of energy-efficient & low-latency deep spiking neural networks for 3D image recognition. *Frontiers in Neuroscience*, 16, 2022b. URL https://www.frontiersin.org/articles/10.3389/fnins.2022.815258.

Gourav Datta, Souvik Kundu, Zihan Yin, Joe Mathai, Zeyu Liu, Zixu Wang, Mulin Tian, Shunlin Lu, Ravi T. Lakkireddy, Andrew Schmidt, Wael Abd-Almageed, Ajey P. Jacob, Akhilesh R. Jaiswal, and Peter A. Beerel. P2M-DeTrack: Processing-in-Pixel-in-Memory for energy-efficient and real-time multi-object detection and tracking. *arXiv preprint arXiv:2205.14285*, 2022c.

Gourav Datta, Zihan Yin, Ajey Jacob, Akhilesh R. Jaiswal, and Peter A. Beerel. Toward efficient hyperspectral image processing inside camera pixels. *arXiv preprint arXiv:2203.05696*, 2022d.

Gourav Datta, Haoqin Deng, Robert Aviles, Zeyu Liu, and Peter A. Beerel. Bridging the gap between spiking neural networks & lstms for latency & energy efficiency. In *2023 IEEE/ACM International Symposium on Low Power Electronics and Design (ISLPED)*, pp. 1–6, 2023a. doi: 10.1109/ISLPED58423.2023.10244298.

Gourav Datta, Zeyu Liu, James Diffenderfer, Bhavya Kailkhura, and Peter A. Beerel. When bio-inspired computing meets deep learning: Low-latency, accurate, & energy-efficient spiking neural networks from artificial neural networks. *arXiv preprint arXiv:2312.06900*, 2023b.

Gourav Datta, Zeyu Liu, Md Abdullah-Al Kaiser, Souvik Kundu, Joe Mathai, Zihan Yin, Ajey P. Jacob, Akhilesh R. Jaiswal, and Peter A. Beerel. In-sensor & neuromorphic computing are all you need for energy efficient computer vision. In *ICASSP 2023 - 2023 IEEE International Conference on Acoustics, Speech and Signal Processing (ICASSP)*, pp. 1–5, 2023c. doi: 10.1109/ICASSP49357.2023.10094902.

Gourav Datta et al. Training energy-efficient deep spiking neural networks with single-spike hybrid input encoding. In *2021 International Joint Conference on Neural Networks (IJCNN)*, volume 1, pp. 1–8, 2021. doi: 10.1109/IJCNN52387.2021.9534306.

J. Deng, W. Dong, R. Socher, L.-J. Li, K. Li, and L. Fei-Fei. ImageNet: A Large-Scale Hierarchical Image Database. In *CVPR09*, 2009.

Shikuang Deng, Yuhang Li, Shanghang Zhang, and Shi Gu. Temporal efficient training of spiking neural network via gradient re-weighting. In *International Conference on Learning Representations*, 2022. URL `https://openreview.net/forum?id=_XNtisL32jv`.

Shikuang Deng, Hao Lin, Yuhang Li, and Shi Gu. Surrogate module learning: Reduce the gradient error accumulation in training spiking neural networks. In Andreas Krause, Emma Brunskill, Kyunghyun Cho, Barbara Engelhardt, Sivan Sabato, and Jonathan Scarlett (eds.), *Proceedings of the 40th International Conference on Machine Learning*, volume 202 of *Proceedings of Machine Learning Research*, pp. 7645–7657. PMLR, 23–29 Jul 2023. URL `https://proceedings.mlr.press/v202/deng23d.html`.

Shikuang Deng et al. Optimal conversion of conventional artificial neural networks to spiking neural networks. In *International Conference on Learning Representations*, 2021.

James Diffenderfer and Bhavya Kailkhura. Multi-prize lottery ticket hypothesis: Finding accurate binary neural networks by pruning a randomly weighted network. In *International Conference on Learning Representations*, 2021. URL `https://openreview.net/forum?id=U_mat0b9iv`.

Ruizhou Ding, Ting-Wu Chin, Zeye Liu, and Diana Marculescu. Regularizing activation distribution for training binarized deep networks. In *2019 IEEE/CVF Conference on Computer Vision and Pattern Recognition (CVPR)*, pp. 11400–11409, 2019. doi: 10.1109/CVPR.2019.01167.

Chaoteng Duan, Jianhao Ding, Shiyan Chen, Zhaofei Yu, and Tiejun Huang. Temporal effective batch normalization in spiking neural networks. In Alice H. Oh, Alekh Agarwal, Danielle Belgrave, and Kyunghyun Cho (eds.), *Advances in Neural Information Processing Systems*, 2022. URL `https://openreview.net/forum?id=fLIgyyQiJqz`.

M. Everingham, L. Van Gool, C. K. I. Williams, J. Winn, and A. Zisserman. The pascal visual object classes (voc) challenge. *International Journal of Computer Vision*, 88(2):303–338, June 2010.

Sieger Falkena, Hadi Jamali-Rad, and Jan van Gemert. Lab: Learnable activation binarizer for binary neural networks. In *Proceedings of the IEEE/CVF Winter Conference on Applications of Computer Vision (WACV)*, pp. 6425–6434, January 2023.

Wei Fang, Zhaofei Yu, Yanqi Chen, Timothee Masquelier, Tiejun Huang, and Yonghong Tian. Incorporating learnable membrane time constant to enhance learning of spiking neural networks. *arXiv preprint arXiv:2007.05785*, 2020.

Wei Fang, Zhaofei Yu, Yanqi Chen, Tiejun Huang, Timothée Masquelier, and Yonghong Tian. Deep residual learning in spiking neural networks. In M. Ranzato, A. Beygelzimer, Y. Dauphin, P.S. Liang, and J. Wortman Vaughan (eds.), *Advances in Neural Information Processing Systems*, volume 34, pp. 21056–21069. Curran Associates, Inc., 2021. URL https://proceedings.neurips.cc/paper/2021/file/afe434653a898da20044041262b3ac74-Paper.pdf.

Charlotte Frenkel, Martin Lefebvre, Jean-Didier Legat, and David Bol. A 0.086-mm^2 12.7-pj/sop 64k-synapse 256-neuron online-learning digital spiking neuromorphic processor in 28-nm cmos. *IEEE Transactions on Biomedical Circuits and Systems*, 13(1):145–158, 2019. doi: 10.1109/TBCAS.2018.2880425.

Xue Geng, Jiawei Hu, Jie Lin, Zhe Wang, Shaohua Li, Min Wu, and Mohamed M. Sabry Aly. MABA-net: Masked additive binary activation network, 2023. URL https://openreview.net/forum?id=LlWfawcSpf.

Kaiming He, Xiangyu Zhang, Shaoqing Ren, and Jian Sun. Delving deep into rectifiers: Surpassing human-level performance on imagenet classification. *arXiv preprint arXiv:1502.01852*, 2015.

Kaiming He, Xiangyu Zhang, Shaoqing Ren, and Jian Sun. Deep residual learning for image recognition. In *Proceedings of the IEEE conference on computer vision and pattern recognition*, pp. 770–778, 2016.

Patrik O Hoyer. Non-negative matrix factorization with sparseness constraints. *Journal of machine learning research*, 5(9), 2004.

Jie Hu, Ziheng Wu, Vince Tan, Zhilin Lu, Mengze Zeng, and Enhua Wu. Elastic-link for binarized neural networks. *Proceedings of the AAAI Conference on Artificial Intelligence*, 36(1):942–950, Jun. 2022. doi: 10.1609/aaai.v36i1.19977. URL https://ojs.aaai.org/index.php/AAAI/article/view/19977.

Hyungjun Kim, Jihoon Park, Changhun Lee, and Jae-Joon Kim. Improving accuracy of binary neural networks using unbalanced activation distribution. In *Proceedings of the IEEE/CVF Conference on Computer Vision and Pattern Recognition (CVPR)*, pp. 7862–7871, June 2021.

Seijoon Kim, Seongsik Park, Byunggook Na, and Sungroh Yoon. Spiking-yolo: Spiking neural network for energy-efficient object detection, 2019.

Youngeun Kim and Priyadarshini Panda. Optimizing deeper spiking neural networks for dynamic vision sensing. *Neural Networks*, 144:686–698, 2021. ISSN 0893-6080. doi: https://doi.org/10.1016/j.neunet.2021.09.022. URL https://www.sciencedirect.com/science/article/pii/S0893608021003841.

Youngeun Kim, Joshua Chough, and Priyadarshini Panda. Beyond classification: Directly training spiking neural networks for semantic segmentation. *Neuromorphic Computing and Engineering*, 2022. URL http://iopscience.iop.org/article/10.1088/2634-4386/ac9b86.

Diederik P Kingma and Jimmy Ba. Adam: A method for stochastic optimization. *arXiv preprint arXiv:1412.6980*, 2014.

Alex Krizhevsky. Learning multiple layers of features from tiny images, 2009. URL https://www.cs.toronto.edu/~kriz/learning-features-2009-TR.pdf.

Mark Kurtz, Justin Kopinsky, Rati Gelashvili, Alexander Matveev, John Carr, Michael Goin, William Leiserson, Sage Moore, Nir Shavit, and Dan Alistarh. Inducing and exploiting activation sparsity for fast inference on deep neural networks. In Hal Daumé III and Aarti Singh (eds.), *Proceedings of the 37th International Conference on Machine Learning*, volume 119 of *Proceedings of Machine Learning Research*, pp. 5533–5543. PMLR, 13–18 Jul 2020. URL https://proceedings.mlr.press/v119/kurtz20a.html.

Changhun Lee, Hyungjun Kim, Eunhyeok Park, and Jae-Joon Kim. Insta-bnn: Binary neural network with instance-aware threshold, 2022.

Jeong-Jun Lee and Peng Li. Reconfigurable dataflow optimization for spatiotemporal spiking neural computation on systolic array accelerators. In *2020 IEEE 38th International Conference on Computer Design (ICCD)*, volume 1, pp. 57–64, 2020. doi: 10.1109/ICCD50377.2020.00027.

Jun Haeng Lee et al. Training deep spiking neural networks using backpropagation. *Frontiers in Neuroscience*, 10, 2016.

Yuhang Li, Yufei Guo, Shanghang Zhang, Shikuang Deng, Yongqing Hai, and Shi Gu. Differentiable spike: Rethinking gradient-descent for training spiking neural networks. In M. Ranzato, A. Beygelzimer, Y. Dauphin, P.S. Liang, and J. Wortman Vaughan (eds.), *Advances in Neural Information Processing Systems*, volume 34, pp. 23426–23439. Curran Associates, Inc., 2021a. URL `https://proceedings.neurips.cc/paper/2021/file/c4ca4238a0b923820dcc509a6f75849b-Paper.pdf`.

Yuhang Li, Yufei Guo, Shanghang Zhang, Shikuang Deng, Yongqing Hai, and Shi Gu. Differentiable spike: Rethinking gradient-descent for training spiking neural networks. In A. Beygelzimer, Y. Dauphin, P. Liang, and J. Wortman Vaughan (eds.), *Advances in Neural Information Processing Systems*, 2021b. URL `https://openreview.net/forum?id=H4e7mBnC9f0`.

Yuhang Li, Youngeun Kim, Hyoungseob Park, Tamar Geller, and Priyadarshini Panda. Neuromorphic data augmentation for training spiking neural networks. *arXiv preprint arXiv:2002.10064*, 2022.

Mingbao Lin, Rongrong Ji, Zihan Xu, Baochang Zhang, Fei Chao, Chia-Wen Lin, and Ling Shao. Siman: Sign-to-magnitude network binarization. *IEEE Transactions on Pattern Analysis and Machine Intelligence*, 45(5):6277–6288, 2023. doi: 10.1109/TPAMI.2022.3212615.

Tsung-Yi Lin, Priya Goyal, Ross Girshick, Kaiming He, and Piotr Dollár. Focal loss for dense object detection. *arXiv preprint arXiv:1708.02002*, 2017a.

Xiaofan Lin, Cong Zhao, and Wei Pan. Towards accurate binary convolutional neural network. In I. Guyon, U. Von Luxburg, S. Bengio, H. Wallach, R. Fergus, S. Vishwanathan, and R. Garnett (eds.), *Advances in Neural Information Processing Systems*, volume 30. Curran Associates, Inc., 2017b. URL `https://proceedings.neurips.cc/paper_files/paper/2017/file/b1a59b315fc9a3002ce38bbe070ec3f5-Paper.pdf`.

Zechun Liu, Baoyuan Wu, Wenhan Luo, Xin Yang, Wei Liu, and Kwang-Ting Cheng. Bi-real net: Enhancing the performance of 1-bit cnns with improved representational capability and advanced training algorithm. In *Proceedings of the European Conference on Computer Vision (ECCV)*, September 2018a.

Zechun Liu, Baoyuan Wu, Wenhan Luo, Xin Yang, Wei Liu, and Kwang-Ting Cheng. Bi-real net: Enhancing the performance of 1-bit cnns with improved representational capability and advanced training algorithm. In *Proceedings of the European Conference on Computer Vision (ECCV)*, pp. 722–737, 2018b.

Zechun Liu, Zhiqiang Shen, Marios Savvides, and Kwang-Ting Cheng. Reactnet: Towards precise binary neural network with generalized activation functions. In *European Conference on Computer Vision (ECCV)*, 2020a.

Zechun Liu, Zhiqiang Shen, Marios Savvides, and Kwang-Ting Cheng. Reactnet: Towards precise binary neural network with generalized activation functions. In *European conference on computer vision*, pp. 143–159. Springer, 2020b.

Qingyan Meng, Mingqing Xiao, Shen Yan, Yisen Wang, Zhouchen Lin, and Zhi-Quan Luo. Training high-performance low-latency spiking neural networks by differentiation on spike representation. In *Proceedings of the IEEE/CVF Conference on Computer Vision and Pattern Recognition (CVPR)*, pp. 12444–12453, June 2022.

E. O. Neftci, H. Mostafa, and F. Zenke. Surrogate gradient learning in spiking neural networks: Bringing the power of gradient-based optimization to spiking neural networks. *IEEE Signal Processing Magazine*, 36(6):51–63, 2019.

Fabrizio Ottati, Chang Gao, Qinyu Chen, Giovanni Brignone, Mario R. Casu, Jason K. Eshraghian, and Luciano Lavagno. To spike or not to spike: A digital hardware perspective on deep learning acceleration. *arXiv preprint arXiv:2306.15749*, 2023.

Priyadarshini Panda and Kaushik Roy. Unsupervised regenerative learning of hierarchical features in spiking deep networks for object recognition. *arXiv preprint arXiv:1602.01510*, 2016.

Mohammad Rastegari, Vicente Ordonez, Joseph Redmon, and Ali Farhadi. Xnor-net: Imagenet classification using binary convolutional neural networks. In *European conference on computer vision*, pp. 525–542. Springer, 2016.

Nitin Rathi et al. DIET-SNN: Direct input encoding with leakage and threshold optimization in deep spiking neural networks. *arXiv preprint arXiv:2008.03658*, 2020a.

Nitin Rathi et al. Enabling deep spiking neural networks with hybrid conversion and spike timing dependent backpropagation. *arXiv preprint arXiv:2005.01807*, 2020b.

Shaoqing Ren, Kaiming He, Ross Girshick, and Jian Sun. Faster r-cnn: Towards real-time object detection with region proposal networks. *Advances in neural information processing systems*, 28, 2015.

Charbel Sakr, Jungwook Choi, Zhuo Wang, Kailash Gopalakrishnan, and Naresh Shanbhag. True gradient-based training of deep binary activated neural networks via continuous binarization. In *2018 IEEE International Conference on Acoustics, Speech and Signal Processing (ICASSP)*, volume 1, pp. 2346–2350, 2018. doi: 10.1109/ICASSP.2018.8461456.

Abhronil Sengupta et al. Going deeper in spiking neural networks: VGG and residual architectures. *Frontiers in Neuroscience*, 13:95, 2019.

Xulong Shi, Zhi Qi, Jiaxuan Cai, Keqi Fu, Yaru Zhao, Zan Li, Xuanyu Liu, and Hao Liu. Repbnn: towards a precise binary neural network with enhanced feature map via repeating. *arXiv preprint arXiv:2207.09049*, 2022.

Karen Simonyan and Andrew Zisserman. Very deep convolutional networks for large-scale image recognition. *arXiv preprint arXiv:1409.1556*, 2014.

Dewei Wang, Pavan Kumar Chundi, Sung Justin Kim, Minhao Yang, Joao Pedro Cerqueira, Joonsung Kang, Seungchul Jung, Sangjoon Kim, and Mingoo Seok. Always-on, sub-300-nw, event-driven spiking neural network based on spike-driven clock-generation and clock- and power-gating for an ultra-low-power intelligent device. In *2020 IEEE Asian Solid-State Circuits Conference (A-SSCC)*, volume 1, pp. 1–4, 2020a. doi: 10.1109/A-SSCC48613.2020.9336139.

Peisong Wang, Xiangyu He, Gang Li, Tianli Zhao, and Jian Cheng. Sparsity-inducing binarized neural networks. *Proceedings of the AAAI Conference on Artificial Intelligence*, 34 (07):12192–12199, Apr. 2020b. URL `https://ojs.aaai.org/index.php/AAAI/article/view/6900`.

Yikai Wang, Wenbing Huang, Yinpeng Dong, Fuchun Sun, and Anbang Yao. Compacting binary neural networks by sparse kernel selection. In *Proceedings of the IEEE/CVF Conference on Computer Vision and Pattern Recognition (CVPR)*, pp. 24374–24383, June 2023.

Ziwei Wang, Ziyi Wu, Jiwen Lu, and Jie Zhou. Bidet: An efficient binarized object detector. In *Proceedings of the IEEE/CVF Conference on Computer Vision and Pattern Recognition (CVPR)*, June 2020c.

Mingqing Xiao, Qingyan Meng, Zongpeng Zhang, Di He, and Zhouchen Lin. Online training through time for spiking neural networks. In S. Koyejo, S. Mohamed, A. Agarwal, D. Belgrave, K. Cho, and A. Oh (eds.), *Advances in Neural Information Processing Systems*, volume 35, pp. 20717–20730. Curran Associates, Inc., 2022. URL `https://proceedings.neurips.cc/paper_files/paper/2022/file/82846e19e6d42ebfd4ace4361def29ae-Paper-Conference.pdf`.

Yixing Xu, Kai Han, Chang Xu, Yehui Tang, Chunjing XU, and Yunhe Wang. Learning frequency domain approximation for binary neural networks. In M. Ranzato, A. Beygelzimer, Y. Dauphin, P.S. Liang, and J. Wortman Vaughan (eds.), *Advances in Neural Information Processing Systems*, volume 34, pp. 25553–25565. Curran Associates, Inc., 2021a. URL `https://proceedings.neurips.cc/paper_files/paper/2021/file/d645920e395fedad7bbbed0eca3fe2e0-Paper.pdf`.

Zihan Xu, Mingbao Lin, Jianzhuang Liu, Jie Chen, Ling Shao, Yue Gao, Yonghong Tian, and Rongrong Ji. Recu: Reviving the dead weights in binary neural networks. In *Proceedings of the IEEE/CVF International Conference on Computer Vision (ICCV)*, pp. 5198–5208, October 2021b.

Huanrui Yang, Wei Wen, and Hai Li. Deephoyer: Learning sparser neural network with differentiable scale-invariant sparsity measures. In *International Conference on Learning Representations*, 2020.

Ruokai Yin, Abhishek Moitra, Abhiroop Bhattacharjee, Youngeun Kim, and Priyadarshini Panda. Sata: Sparsity-aware training accelerator for spiking neural networks. *IEEE Transactions on Computer-Aided Design of Integrated Circuits and Systems*, 1(1):1–1, 2022. doi: 10.1109/TCAD.2022.3213211.

Wenrui Zhang and Peng Li. Temporal spike sequence learning via backpropagation for deep spiking neural networks. In H. Larochelle, M. Ranzato, R. Hadsell, M.F. Balcan, and H. Lin (eds.), *Advances in Neural Information Processing Systems*, volume 33, pp. 12022–12033. Curran Associates, Inc., 2020. URL `https://proceedings.neurips.cc/paper/2020/file/8bdb5058376143fa358981954e7626b8-Paper.pdf`.

Yichi Zhang, Zhiru Zhang, and Lukasz Lew. Pokebnn: A binary pursuit of lightweight accuracy. In *Proceedings of the IEEE/CVF Conference on Computer Vision and Pattern Recognition (CVPR)*, pp. 12475–12485, June 2022.

Hanle Zheng, Yujie Wu, Lei Deng, Yifan Hu, and Guoqi Li. Going deeper with directly-trained larger spiking neural networks. *Proceedings of the AAAI Conference on Artificial Intelligence*, 35 (12):11062–11070, May 2021. doi: 10.1609/aaai.v35i12.17320. URL `https://ojs.aaai.org/index.php/AAAI/article/view/17320`.

Pengju Ren Zhijun Tu, Xinghao Chen and Yunhe Wang. Adabin: Improving binary neural networks with adaptive binary sets. In *European Conference on Computer Vision (ECCV)*, 2022a.

Pengju Ren Zhijun Tu, Xinghao Chen and Yunhe Wang. Adabin: Improving binary neural networks with adaptive binary sets. In *European Conference on Computer Vision (ECCV)*, 2022b.

A Appendix

A.1 Threshold & Weight Updates due to Hoyer Loss

For a hidden layer l, the weight update is computed as

$$\begin{aligned}\Delta W_l = \frac{\partial L_{CE}}{\partial \boldsymbol{w}_l} + \lambda_H \frac{\partial L_H}{\partial \boldsymbol{w}_l} = \frac{\partial L_{CE}}{\partial \boldsymbol{o}_l}\frac{\partial \boldsymbol{o}_l}{\partial \boldsymbol{z}_l}\frac{\partial \boldsymbol{z}_l}{\partial \boldsymbol{u}_l}\frac{\partial \boldsymbol{u}_l}{\partial \boldsymbol{w}_l} \\ + \lambda_H \frac{\partial L_H}{\partial \boldsymbol{u}_l}\frac{\partial \boldsymbol{u}_l}{\partial \boldsymbol{w}_l} = \frac{\partial L_{CE}}{\partial \boldsymbol{o}_l}\frac{\partial \boldsymbol{o}_l}{\partial \boldsymbol{z}_l}\frac{\boldsymbol{o}_{l-1}}{v_l^{th}} + \lambda_H \frac{\partial L_H}{\partial \boldsymbol{u}_l}\boldsymbol{o}_{l-1}\end{aligned} \tag{9}$$

where $\frac{\partial L_H}{\partial \boldsymbol{u}_l}$ can be computed as

$$\begin{aligned}\frac{\partial L_H}{\partial \boldsymbol{u}_l} &= \frac{\partial L_H}{\partial \boldsymbol{u}_{l+1}}\frac{\partial \boldsymbol{u}_{l+1}}{\partial \boldsymbol{o}_l}\frac{\partial \boldsymbol{o}_l}{\partial \boldsymbol{z}_l}\frac{\partial \boldsymbol{z}_l}{\partial \boldsymbol{u}_l} + \frac{\partial H(\boldsymbol{z}_l^{clip})}{\partial \boldsymbol{u}_l} \\ &= \frac{\partial L_H}{\partial \boldsymbol{u}_{l+1}}\boldsymbol{w}_{l+1}\frac{\partial \boldsymbol{o}_l}{\partial \boldsymbol{z}_l}\frac{1}{v_l^{th}} + \frac{\partial H(\boldsymbol{z}_l^{clip})}{\partial \boldsymbol{z}_l^{clip}}\frac{\partial \boldsymbol{z}_l^{clip}}{\partial \boldsymbol{z}_l}\frac{1}{v_l^{th}}\end{aligned} \tag{10}$$

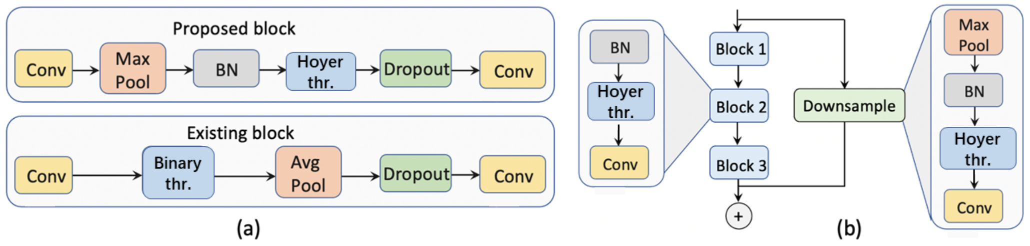

Figure 3: BANN architectures corresponding to (a) VGG and (b) ResNet based models.

This is because L_H is the sum of the Hoyer regularizer of the first $l-1$ layers, the lth layer, and the layers after the lth layer. While computing $\frac{\partial L_H}{\partial \boldsymbol{u}_l}$, the gradient of the 1^{st} part is 0, and the gradient of the 2^{nd} (3^{rd}) part is captured in the second (first) term in Eq. 8. Note that $\frac{\partial L_H}{\partial \boldsymbol{u}_{l+1}}$ is the gradient backpropagated from the $(l+1)^{th}$ layer, that is iteratively computed from the last layer L (see Eqs. 7 and 11). Also, note that for any hidden layer l, there are two gradients that contribute to the Hoyer loss with respect to the activation $\boldsymbol{u}_l$; one is from the subsequent layer $(l+1)$ and the other is directly from its Hoyer regularizer. Similarly, $\frac{\partial L_{CE}}{\partial \boldsymbol{o}_l}$ is computed iteratively, starting from the penultimate layer $(L-1)$ defined in Eq. 7, as follows.

$$\frac{\partial L_{CE}}{\partial \boldsymbol{o}_l}=\frac{\partial L_{CE}}{\partial \boldsymbol{o}_{l+1}}\frac{\partial \boldsymbol{o}_{l+1}}{\partial \boldsymbol{z}_{l+1}}\frac{\partial \boldsymbol{z}_{l+1}}{\partial \boldsymbol{u}_{l+1}}\frac{\partial \boldsymbol{u}_{l+1}}{\partial \boldsymbol{o}_l}=\frac{\partial L_{CE}}{\partial \boldsymbol{o}_{l+1}}\frac{\partial \boldsymbol{o}_{l+1}}{\partial \boldsymbol{z}_{l+1}}\frac{\boldsymbol{w}_{l+1}}{v_l^{th}} \tag{11}$$

Finally, the threshold update for the hidden layer l is computed as

$$\begin{aligned}\Delta v_l^{th}&=\frac{\partial L_{CE}}{\partial v_l^{th}}+\lambda_H\frac{\partial L_H}{\partial v_l^{th}}=\frac{\partial L_{CE}}{\partial \boldsymbol{o}_l}\frac{\partial \boldsymbol{o}_l}{\partial \boldsymbol{z}_l}\frac{\partial \boldsymbol{z}_l}{\partial v_l^{th}}+\lambda_H\frac{\partial L_H}{\partial v_l^{th}}\\&=\frac{\partial L_{CE}}{\partial \boldsymbol{o}_l}\frac{\partial \boldsymbol{o}_l}{\partial \boldsymbol{z}_l}\frac{-\boldsymbol{u}_l}{(v_l^{th})^2}+\lambda_H\frac{\partial L_H}{\partial \boldsymbol{u}_{l+1}}\frac{\partial \boldsymbol{u}_{l+1}}{\partial v_l^{th}}\end{aligned} \tag{12}$$

$$\frac{\partial \boldsymbol{u}_{l+1}}{\partial v_l^{th}}=\frac{\partial \boldsymbol{u}_{l+1}}{\partial \boldsymbol{o}_l}\cdot\frac{\partial \boldsymbol{o}_l}{\partial v_l^{th}}=\boldsymbol{w}_{l+1}\cdot\frac{\partial \boldsymbol{o}_l}{\partial \boldsymbol{z}_l}\cdot\frac{-\boldsymbol{u}_l}{(v_l^{th})^2} \tag{13}$$

Note that we use this v_l^{th}, which is updated in each iteration, to estimate the threshold in our BANN model using Eq. 4.

A.2 Network Architecture

We adopt a series of network architectural tricks for our BANNs (Datta & Beerel, 2022; Chowdhury et al., 2021; Rathi et al., 2020a). As shown in Fig. 3(a), for the VGG variant, we use the max pooling layer immediately after the convolutional layer that is common in many BNN architectures (Rastegari et al., 2016), and introduce the BN layer after max pooling. Similar to recently developed multi-time-step SNN models (Zheng et al., 2021; Li et al., 2021a; Deng et al., 2022; Meng et al., 2022), we observe that BN helps increase the test accuracy with one time step. In contrast, for the ResNet variants, inspired by (Liu et al., 2018b), we observe models with shortcuts that bypass every block can also further improve the performance of the SNN. We also observe that the sequence of BN layer, Hoyer spike layer, and convolution layer outperforms the original bottleneck in ResNet. More details are shown in Fig. 3(b).

A.3 Ablation Studies

We conduct ablation studies to analyze the contribution of each technique in our proposed approach. For fairness, we train all the ablated models on CIFAR10 dataset for 400 epochs, and use Adam as the optimizer, with 0.0001 as the initial learning rate. Our results are shown in Table 8, where the model without Hoyer threshold layer indicates that we set the threshold as v_l^{th} similar to existing works (Datta & Beerel, 2022; Rathi et al., 2020a) rather than our proposed Hoyer extremum.

Table 8: Ablation study of the different methods in our proposed training framework on CIFAR10.

Arch.	Hoyer Reg.	Hoyer Spike	Acc. (%)	Sparsity (%)
VGG16	×	×	88.42	84.38
VGG16	✓	×	90.45	79.52
VGG16	×	✓	92.90	78.30
VGG16	✓	✓	**93.13**	77.43
ResNet34	×	×	87.41	77.22
ResNet18	✓	×	90.95	79.50
ResNet18	×	✓	91.17	74.13
ResNet18	✓	✓	**91.48**	74.17

Table 9: Comparison of our BANNs with full-precision DNNs & BNNs on VOC2007 dataset.

Framework	Backbone	mAP(%)
Faster R-CNN	Original ResNet50	79.5
Faster R-CNN	Bi-Real (Liu et al., 2018b)	65.7
Faster R-CNN	ReActNet (Liu et al., 2020b)	73.1
Faster R-CNN	BANN ResNet50	73.7
Retinanet	Original ResNet50	77.3
Retinanet	BANN ResNet50 (ours)	70.5
YOLO	BANN DarkNet (Kim et al., 2019)	53.01
SSD	BNN VGG16 (Wang et al., 2020c)	66.0

With VGG16, our Hoyer regularizer approach leads to a 2.03% increase in accuracy. Together, with our Hoyer threshold layer, the accuracy improves by 2.68% to 93.13% while also yielding a 2.09% reduction in sparsity.

We observe a similar trend for our network modifications and Hoyer threshold layer with ResNet18. However, Hoyer regularizer in this case also increases the sparsity from 72.38% to 77.22% to 79.50%, while also negligibly reducing the accuracy. In summary, the combination of our Hoyer regularizer and Hoyer threshold layer yield the SOTA BNN/SNN performance.

A.4 Object Detection Results

Object Detection Results: For object detection on VOC2007, we compare the performance obtained by our BANN models with full-precision DNNs and BNNs in Table 9. For two-stage architectures, such as Faster R-CNN, the mAP of our BANN models surpass the existing BNNs by >0.6%. For one-stage architectures, such as RetinaNet (chosen because of its SOTA performance), our BANN models with a ResNet50 backbone yields a mAP of 70.5% (highest among existing BNN, SNN, AddNNs). Note that our BANN-based VGG and ResNet-based backbones lead to a significant drop in mAP with the YOLO framework that is more compatible with the DarkNet backbone (even existing DarkNet-based SNNs lead to very low mAP with YOLO as shown in Table 9).

A.5 Proof of threshold downscaling with Hoyer extremum

In order to prove that our Hoyer regularized threshold is always less than or equal to the trainable threshold v^{th}, we first prove that the Hoyer extremum of $\boldsymbol{z}_l^{clip}$ is less than or equal to 1. Let us use $\boldsymbol{c}_l$ to represent $\boldsymbol{z}_l^{clip}$, so $\forall j, 0 \leq c_l^j \leq 1$

$$\begin{aligned} Ext(\boldsymbol{c}_l) &= \frac{\|\boldsymbol{c}_l\|_2^2}{\|\boldsymbol{c}_l\|_1} = \frac{\sum_j (c_l^j)^2}{\sum_j c_l^j} \\ &\leq \frac{\sum_j (c_l^j \cdot max(c_l^j))}{\sum_j c_l^j} \leq max(c_l^j)) \leq 1 \end{aligned} \tag{14}$$

Table 10: Comparison of our one- and multi-time-step SNN models to existing SNN models on DVS-CIFAR10 and IBM-Gesture datasets.*Results are based on our replicated implementation.

Dataset	Reference	Training	Architecture	Acc. (%)	T.S.
DVS-CIFAR10	(Deng et al., 2022)	TET	VGGSNN	83.17 75.20*	10 4*
	(Li et al., 2022)	tdBN+NDA	VGG11	81.7	10
	(Kim & Panda, 2021)	SALT+Switched BN	VGG16	67.1	20
	This work	Hoyer reg.	VGGSNN	**83.68** **76.17**	10 4
N-CalTech101	(Li et al., 2022)	tdBN+NDA	VGG11	78.6	10
	(Kim & Panda, 2021)	SALT+Switched BN	VGG16	55.0	20
	This work	Hoyer reg.	VGG11	**79.92**	10

So the Hoyer extremum of $\boldsymbol{z}_l^{clip}$ is always less than or equal one, and thus, our Hoyer regularized threshold, which is the product of v_l^{th} and $Ext(\boldsymbol{z}_l^{clip})$ is always less than or equal to the trainable threshold v_l^{th}.

A.6 Datasets & Hyperparameters

For training VGG16 models, we using Adam optimizer with initial learning rate of 0.0001, weight decay of 0.0001, dropout of 0.1 and batch size of 128 in CIFAR10 for 600 epochs, and Adam optimizer with weight decay of $5e{-}6$ and with batch size 64 in ImageNet for 180 epochs. For training ResNet models, we using SGD optimizer with initial learning rate of 0.1, weight decay of 0.0001 and batch size of 128 in CIFAR10 for 400 epochs, and Adam optimizer with weight decay of $5e{-}6$ and with batch size 64 in ImageNet for 120 epochs. We divide the learning rate by 5 at 60%, 80%, and 90% of the total number of epochs. Note that $\lambda_h = 1e{-}8$ for all our experiments.

When calculating the Hoyer extremum we implement two versions, one that calculates the Hoyer extremum for the whole batch, while another that calculates it channel-wise. Our experiments show that using the channel-wise version can bring $0.1{-}0.3\%$ increase in accuracy. All the experimental results reported in this paper use this channel-wise version.

For Faster R-CNN, we use SGD optimizer with initial learning rate of 0.01 for 50 epochs, and divide the learning rate by 10 after 25 and 40 epochs each. For Retinanet, we use SGD optimizer with initial learning rate of 0.001 with the same learning rate scheduler as Faster R-CNN.

A.7 Extension to SNNs for Dynamic Vision Sensor (DVS) tasks

The inherent temporal dynamics in SNNs may be better leveraged in DVS or event-based tasks (Deng et al., 2022; Li et al., 2022; Kim & Panda, 2021; Kim et al., 2022) compared to standard static vision tasks. Hence, we also evaluate our framework on two DVS datasets, namely DVS-CIFAR10 and IBM-Gesture. As illustrated in Table 10, we surpass the test accuracy of existing works (Li et al., 2022; Kim & Panda, 2021) by 0.93% on average at iso-time-step and architecture. Note that the architecture VGGSNN employed in our work and (Deng et al., 2022) is based on VGG11 with two fully connected layers removed as (Deng et al., 2022) found that additional fully connected layers were unnecessary for neuromorphic datasets. To compensate for the loss of momentum in SGD and improve the accuracy, we adopt the temporal efficient training (TET) method in our framework (Deng et al., 2022). In fact, our accuracy gain is more significant at low time steps, thereby implying the portability of our approach to DVS tasks. Note that similar to static datasets, a large number of time steps increase the temporal overhead in SNNs, resulting in a large memory footprint and spiking activity.

A.8 Energy Evaluation Framework

A.8.1 Compute Energy

The total compute energy (CE) of a BANN ($BANN_{CE}$) can be estimated as

$$BANN_{CE}{=}DNN_1^{op}E_{mac}{+}\sum_{l=2}^{L}(S_l DNN_l^{op}E_{ac}+E_{sp}DNN_l^{op}){+}\sum_{l=1}^{L}DNN_l^{com}E_{com} \tag{15}$$

because BANN receives full-precision input in the first layer (l=1) without any sparsity (Chowdhury et al., 2021; Datta et al., 2022b; Rathi et al., 2020a). Note that DNN_l^{com} denotes the total number of comparison (thresholding) operations in the layer l with each operation consuming 1.64pJ energy in our FPGA platform for FP repreresentation. Also, note that DNN_l^{op} denote the total number of floating point (MAC or AC) operations in layer l, where each FP MAC operation consumes 13.32pJ energy, while each FP AC operation consumes 1.8pJ energy. Lastly, S_l denote the spiking activity in the layer l, and $E_{sp} = 0.05$pJ denotes the energy overhead due to sparsity, that is incurred in checking whether the binary activation is zero.

The CE of the full-precision DNN (DNN_{CE}) and bi-polar BNN (BNN_{CE}) is estimated as

$$DNN_{CE} = \sum_{l=1}^{L} DNN_l^{op} E_{mac}, \quad BNN_{CE} = DNN_1^{op} E_{mac} + \sum_{l=2}^{L} DNN_l^{op} E_{xor} \tag{16}$$

where we ignore the energy consumed by the ReLU operation (significantly lower compared to thresholding operation) since that includes only checking the sign bit. Note that E_{xor} denotes the XOR energy incurred in the binary convolution/linear operations in bi-polar BNNs.

The compute energy of an SNN with a total of T time steps is denoted as

$$SNN_{CE} = \sum_{t=1}^{T} \left(DNN_1^{op} E_{mac} + \sum_{l=2}^{L} (S_l^t DNN_l^{op} E_{ac} + E_{sp} DNN_l^{op}) + \sum_{l=1}^{L} DNN_l^{com} E_{com} \right) \tag{17}$$

where S_l^t denotes the activation sparsity of layer l at time step t, and we replicate the BANN energy for all T time steps. Note that we ignore the potential reset energy since the number of reset operations is negligible compared to the FLOPs, and the energy consumed per reset operation is similar to that of an AC operation.

Intuitively, BANNs with low-bit ($\leq$6-bits) weights, consume lower compute energy compared to BNNs since the energy savings due to the activation sparsity even with its overhead outweighs the energy savings due to XOR operations compared to low-precision AC operations. BANNs also consume lower compute energy compared to SNNs and DNNs due to the higher activation sparsity, leading to less number of FP operations.

A.8.2 Memory Energy

Since memory accesses often dominate the total energy consumption in DNNs, we incorporate the same in our energy model using (Ottati et al., 2023).

The memory energy of a BANN is estimated as

$$\begin{aligned} BANN_{ME} = &\sum_{l=1}^{L} C_l^i C_l^o k_l^2 E_{rd}^{wt} + C_1^i C_1^o k_l^2 H_1 W_1 E_{rd}^{inp} + \\ &\sum_{l=2}^{L} C_l^i C_l^o k_l^2 H_l W_l (S_l E_{rd}^{sp} + E_{sp}) + \sum_{l=1}^{L} H_l W_l C_l^o E_{wr}^{sp} \end{aligned} \tag{18}$$

where C_l^i, C_l^o, k_l, H_l, and W_l denote the number of input channels, number of output channels, kernel size, output feature map height, and output feature map width respectively. Note that E_{rd}^{sp} and E_{wr}^{sp} denote the energy incurred in reading a spike input and writing a spike output respectively from/to the on-chip FPGA memory. On the other hand, E_{rd}^{inp} denotes the read energy of each 8-bit input pixel value, and E_{rd}^{wt} denotes the read energy of the weights from the memory.

The memory energy of a traditional bi-polar BNN is estimated as

$$BNN_{ME} = \sum_{l=1}^{L} C_l^i C_l^o k_l^2 E_{rd}^{wt} + C_1^i C_1^o k_l^2 H_1 W_1 E_{rd}^{inp} + \sum_{l=1}^{L} C_l^i C_l^o k_l^2 H_l W_l E_{rd}^{sp} + \sum_{l=1}^{L} H_l W_l C_l^o E_{wr}^{of} \tag{19}$$

where E_{wr}^{of} denotes the energy incurred in writing the FP output feature map to the on-chip memory. While E_{rd}^{wt} is lower for BNNs compared to multi-bit-weighted BANNs, BNNs incur higher output

Table 11: Comparison of the different compute and memory energy numbers for FP weights and membrane potentials obtained from our post place-and-route FPGA simulations on 28nm Kintex7 device.

Parameter	Energy (pJ)	Parameter	Energy (pJ)
E_{mac}	13.2	E_{rd}^{wt}=E_{rd}^{mem}	33.4
E_{ac}	1.8	E_{rd}^{inp}	8.6
E_{com}	1.4	E_{rd}^{sp}	1.7
E_{sp}	0.05	E_{wr}^{sp}	3.8
E_{xor}	0.08	E_{wr}^{mem}	40.1

feature map write energy due to multi-bit outputs, and higher input feature map read energy due to absence of spike sparsity.

In summary, BANN can hep reduce both the compute and memory energy compared to BNNs, SNNs, and non-spiking DNNs, provided the hardware supports the activation sparsity.

The memory energy of an SNN with T time steps is estimated as

$$\begin{aligned} SNN_{ME}=&\sum_{l=1}^{L} C_l^i C_l^o k_l^2 E_{rd}^{wt} + C_1^i C_1^o k_l^2 H_1 W_1 E_{rd}^{inp} + \\ &\sum_{t=1}^{T}\left(\sum_{l=2}^{L} C_l^i C_l^o k_l^2 H_l W_l (S_l^t E_{rd}^{sp} + E_{sp}) + \sum_{l=1}^{L} H_l W_l C_l^o (E_{wr}^{sp} + E_{rd}^{mem} + E_{wr}^{mem})\right) \end{aligned} \tag{20}$$

where E_{rd}^{mem} and E_{wr}^{mem} denote the energies incurred in read and write operations of the membrane potential respectively, that happens for every time step. Lastly, the memory energy of a FP DNN is computed as

$$DNN_{ME}=\sum_{l=1}^{L} C_l^i C_l^o k_l^2 E_{rd}^{wt} + C_1^i C_1^o k_l^2 H_1 W_1 E_{rd}^{inp} + \sum_{l=1}^{L} C_l^i C_l^o k_l^2 H_l W_l E_{rd}^{if} + \sum_{l=1}^{L} H_l W_l C_l^o E_{wr}^{of} \tag{21}$$

where E_{rd}^{if} denotes the read energy of the full-precision input feature map, that is higher than the spike read energy incurred in the BNN/BANN/SNN. Note that all the memory access energy numbers, E_{rd}^{wt}, E_{rd}^{sp}, E_{wr}^{sp}, E_{rd}^{inp}, E_{rd}^{if}, E_{wr}^{of}, E_{rd}^{mem}, E_{wr}^{mem}, are obtained from our FPGA simulation setup with a 42MB of on-chip (BRAM and URAM) capacity. Note that each of these numbers depend on the bit-precision of the value read/written. For example, assuming that 32 spikes are encoded to an 32b memory word, the energy associated with a spike read memory operation is almost same as $\frac{E_{rd}^{wt}}{32}$, for 32-bit FP weights. All these numbers, along with those for the compute operations, are tabulated in Table 11, where the weights, membrane potentials, input and output feature maps have FP representation.

Note that for SNNs, the memory footprint is primarily dominated by the read and write accesses of the post-synaptic potential at each time step (Yin et al., 2022). This is because these memory accesses are not influenced by the SNN sparsity since each post-synaptic potential is the sum of $k^2 c_{in}$ weight-modulated spikes. For a typical convolutional layer, $k = 3$, $c_{in} = 128$, and so it is almost impossible that all the $k^2 c_{in}$ spike values are zero for the membrane potential to be kept unchanged at a particular time step. Note that the number of input (output) feature map read (write) accesses can be reduced with the spike sparsity, and typically do not dominate the memory footprint of SNNs. Since BANNs do not have the temporal membrane potential, they can significantly reduce the memory cost compared to SNNs. Compared to DNNs and BNNs, the memory cost, that is dominated by the feature map accesses (with weight re-use), can be reduced in BANNs by the zero gating logic that leverages spike sparsity.

A.9 TRAINING & INFERENCE TIME REQUIREMENTS

Because SOTA SNNs require iteration over multiple time steps and storage of the membrane potentials for each neuron, their training and inference time can be substantially higher than the DNN/BNN counterparts. Though reducing their latency

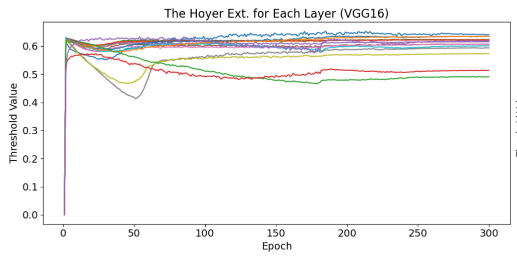

(a) VGG16

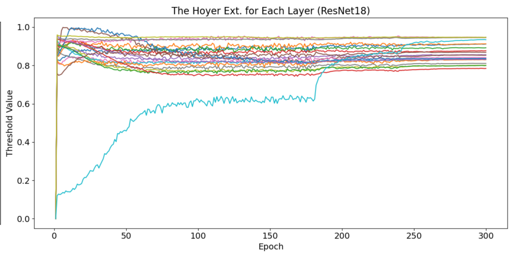

(b) ResNet20

Figure 5: Evolvement of the learned threshold value for each layer of VGG16 and ResNet20 on CIFAR10.

to 1 time step can bridge this gap significantly, as shown in Figure 4, it significantly increases the training complexity due to the iterative time-step reduction. On average, our BANNs represent a $2.38\times$ and $2.33\times$ reduction in training and inference time per epoch respectively, compared to the multi-time-step training approaches (Datta & Beerel, 2022; Rathi et al., 2020a) with iso-batch and hardware conditions.

Compared to the existing one-time-step SNNs (Chowdhury et al., 2021), we yield a $19\times$ and $1.25\times$ reduction in training and inference time. This inference time reduction is possibly due to more efficient PyTorch tensor operations used in our code which may be better optimized using the underlying CUDA compiler. Such significant savings in training time, which translates to power savings in big data centers, can potentially reduce AI's environmental impact.

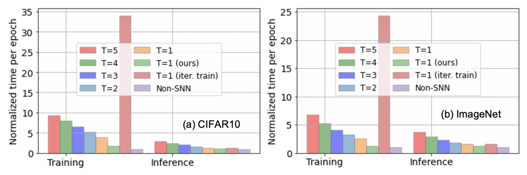

Figure 4: Normalized training and inference time/epoch with iso-batch (256) and hardware (RTX 3090, 24 GB memory) conditions for (a) CIFAR10 and (b) ImageNet with VGG16.

A.10 Comparison of latency footprint

Using a hardware validated latency model on ResNet-18, our 6-bit weighted BANNs incur $1.34\times$ higher latency compared to uni-polar BNNs, as activation sparsity favors energy not latency & popcount incurs lower latency than accumulates. On the contrary, our binary weighted BANNs incur almost similar $(0.96\times)$ latency as a uni-polar BNN.

A.11 Stability of Hoyer Regularized Training

The effect of the Hoyer spike layer is a down-scaling of the thresholds obtained from SGD. However, because these thresholds are fixed during inference, the mapping to neuromorphic hardware is no more complex than a traditional SNN. Moreover, since our training method incorporates the learnable training threshold obtained via SGD, we report its evolvement during the training stage in Fig. 5 (a) and (b) for VGG16 and ResNet20 respectively on CIFAR10. As we can see, our threshold value stabilizes well during the later parts of the training for all the layers, demonstrating the robustness of our method.